

A Young Multipolar Planetary Nebula in the Making – IRAS 21282+5050

Chih-Hao Hsia^{1, 3} • Yong Zhang^{2,3} • Sun Kwok^{3,4}
• Wayne Chau^{3,5}

Email address of corresponding author Sun Kwok:
skwok@eoas.ubc.ca

Abstract We present high-angular-resolution *Hubble Space Telescope* (*HST*) optical and near-infrared imaging of the compact planetary nebula (PN) IRAS 21282+5050. Optical images of this object reveal several complex morphological structures including three pairs of bipolar lobes and an elliptical shell lying close to the plane of the sky. From near-infrared observations, we found a dust torus oriented nearly perpendicular to the major axis of elliptical shell. The results suggest that IRAS 21282+5050 is a multipolar PN, and these structures developed early during the post asymptotic-giant-branch (AGB) evolution. From a three-dimensional (3-D) model, we derived the physical dimensions of these apparent structures. When the 3-D model is viewed from different orientations, IRAS 21282+5050 shows similar apparent structures as other multipolar PNs. Analysis of the spectral energy distribution and optical spectroscopic observations of the nebula suggests the presence of a cool companion to the hot central star responsible for the ionization of the

nebula. Whether the binary nature of the central star has any relations with the multipolar structure of the nebula needs to be further investigated.

1 Introduction

Planetary nebulae (PNs) are traditionally known for their simple spherical, shell-like structures. Their morphological structures are often classified as round, elliptical, or bipolar (Balick 1987). After the development of high-dynamic-range CCD imaging, especially after the launch of the *Hubble Space Telescope* (*HST*), many complex internal structures have been discovered. These include multipolar lobes, circular concentric arcs, two-dimensional (2-D) rings, jets, knots, ansae, extended halos, and equatorial tori.

Multipolar nebulae are defined as objects that possess at least two pairs of axial symmetric structures. The first multipolar PN was discovered in the Instituto de Astrofísica de Canarias morphological survey of Galactic PNs (Manchado, Stanghellini, & Guerrero 1996). Five objects (M2-46, K3-24, M1-75, M3-28, M4-14) were identified by Manchado, Stanghellini, & Guerrero (1996) as PNs with quadrupolar structures. Multipolar PN found in subsequent deep and high-dynamic-range optical imaging include Hen 2-47 and M 1-37 (Sahai 2000), NGC 6881 (Kwok & Su 2005), NGC 6072 (Kwok et al. 2010), NGC 6644 (Hsia et al. 2010), NGC 5189 (Sabin et al. 2012), Kn 26 (Guerrero et al. 2013), NGC 6058 (Guillén et al. 2013), NGC 6309 (Rubio et al. 2015), Hen 3-1333 and Hen 2-113 (Danehkar & Parker 2015). Under earlier classification schemes, these objects were classified as “elliptical” and/or “bipolar”. Even large, well-known PN, e.g., NGC 2440 (López et al. 1998) and NGC 7026 (Clark et al. 2013), are now known to be multipolar.

Chih-Hao Hsia

Yong Zhang

Sun Kwok

Wayne Chau

¹State Key Laboratory of Lunar and Planetary Sciences, Macau University of Science and Technology, Taipa, Macau 999078, China

²School of Physics and Astronomy, Sun Yat-Sen University Zhuhai Campus, Tangjia, Zhuhai, 519082, China

³Laboratory for Space Research, The University of Hong Kong, Hong Kong, China

⁴Department of Earth, Ocean, and Atmospheric Sciences, University of British Columbia, Vancouver, Canada

⁵Department of Physics, The University of Hong Kong, Hong Kong, China

Recent classification schemes find 12% of 150 post asymptotic-giant-branch (AGB) stars (Manchado et al. 2011) and 20% of 119 young PNs (Sahai, Morris, & Villar 2011) to be multipolar. A study of multipolar or quadrupolar PNs by Hsia et al. (2014) suggests that these multipolar structures could be the result of interactions between previously ejected AGB winds and later-developed fast winds, the presences of the structures are ascribed to the multiple phases of fast winds separated by time or directional variations. What is the nature and formation of multipolar lobes? Although some studies have discussed this issue (García-Segura 2010; Kwok 2010; Velázquez et al. 2012), the origin and exact physical mechanisms responsible for these structures are still unresolved.

The PN IRAS 21282+5050 (PNG 093.9-00.1, hereafter referred to as IRAS 21282) was first discovered by *Infrared Astronomical Satellite (IRAS)* for its strong infrared emission (UIE) features (7.7, 8.6, 11.3, and 12 μm) in its *IRAS* low-resolution spectra (Cohen, Tielens, & Allamandola 1985; Jourdain de Muizon 1986). These features are part of a family of unidentified infrared emission bands (3.3, 3.4, 6.2, 7.7, 8.6, 11.3, 12.6 μm) commonly seen in carbon-rich PNs and PPNs (Kwok, Volk, & Hrivnak 1999). In addition to common UIE bands, weaker features at 3.46 and 3.52 μm are also seen (Jourdain de Muizon et al. 1986; Jourdain de Muizon, D’Hendecourt, & Geballe 1990; Nagata et al. 1988). High-spectral-resolution observations have identified features at 3.40, 3.46, 3.52 as due to aliphatic C–H stretch of methyl and methylene groups and the 3.45 μm as due to C–H stretch of an aldehydes group (Hrivnak, Geballe & Kwok 2007).

In this paper, we present results of our morphological study for IRAS 21282 based on optical and near-infrared images taken with *HST*. These images reveal the unique morphology and properties of the PN. The observations and data reduction procedures are described in § 2. In § 3 we present the results of imaging and spectroscopy in the optical and near-infrared for this source. From photometric and spectroscopic observations from radio to ultraviolet (UV), we constructed a spectral energy distribution (SED) and discuss the energetics of the central source in § 4. A comparison of our observations with a three-dimensional model are presented in § 5. A discussion of the implications based on a comparison of studied multipolar PNs is given in § 6. Finally, a conclusion is given in § 7.

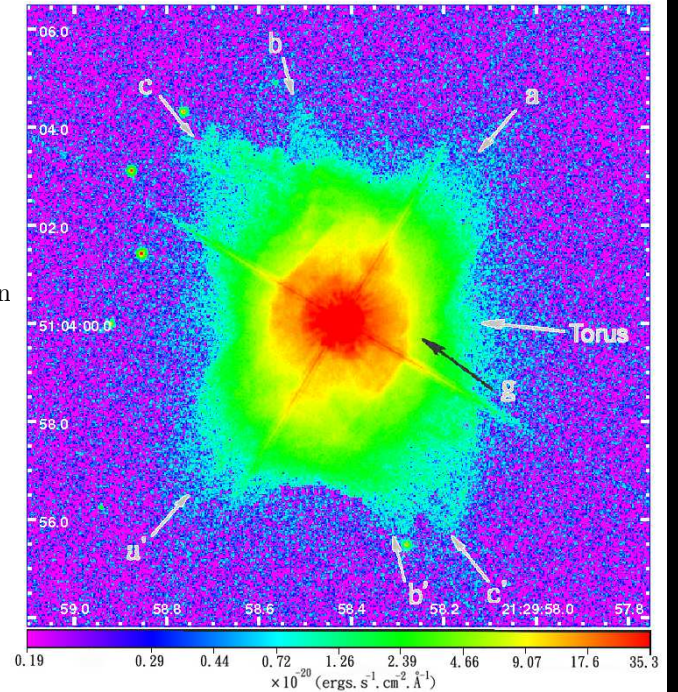


Fig. 1 The complex morphological structure of IRAS 21282+505 is shown in this *HST/ACS* F606W broad-band image. At the center of the nebula is a bright cylindrical shell (labeled “g”). In the outer regions, three pairs of bipolar lobes (marked as $a-a'$, $b-b'$, and $c-c'$) can be identified. Along the E-W direction is an extended region which could be the counterpart of the torus seen in the NICOMS image (Fig. 3). The intensity display is on a logarithmic scale and the scale bar is given at the bottom in units of $\text{ergs cm}^{-2} \text{s}^{-1} \text{\AA}^{-1}$.

Table 1 Log of HST observations for IRAS 21282+5050.

Instrument	Filter	λ_c (Å)	$\Delta\lambda$ (Å)	Exposures (s)	Observation Date	Program ID
Visible						
ACS	F606W	5919	2342	5×1	2002 Dec 07	9463
	F606W	5919	2342	60×1	2002 Dec 07	9463
	F606W	5919	2342	250×2	2002 Dec 07	9463
WFPC2	F656N	6564	22	20×2	1999 Aug 23	8345
	F656N	6564	22	140×2	1999 Aug 23	8345
	F656N	6564	22	400×2	1999 Aug 23	8345
Near-infrared						
NICMOS	F160W	15931	4030	32×12	1997 Sep 21	7365
	F205W	20406	6125	32×12	1997 Sep 21	7365

2 Observations and data reduction

2.1 *HST* optical imaging

We have analyzed the high-resolution optical images on IRAS 21282 retrieved from the Space Telescope Science Archive. The broad-band images were obtained under program 9463 (PI: R. Sahai) using the Advanced Camera for Surveys (ACS) on *HST*. The object was observed with broad F606W (V-band) filter ($\lambda_c = 5919$ Å, $\Delta\lambda = 2342$ Å) on the High Resolution Channel (HRC) on 2002 December 7, which provides a $26'' \times 29''$ field of view (FOV) at a spatial resolution of $0.''027$ pixel⁻¹. The actual observations were made with different exposure times (from 5 s to 250 s) to allow for the imaging of both the bright central region and the faint outer parts.

In addition, we also retrieved narrow-band observations using the Wide Field Planetary Camera 2 (WFPC 2) on *HST* through the observation program 8345 (PI: R. Sahai) on 1999 August 23. The nebula was imaged by the Planetary Camera (PC), which has a FOV of $36.''8 \times 36.''8$ with a pixel scale of $0.''045$ pixel⁻¹. The narrow-band imaging observations were made with narrow-band F656N (H α) filter ($\lambda_c = 6564$ Å, $\Delta\lambda = 22$ Å).

The standard *HST* pipeline calibration has been applied to all data. Successful bias subtraction and flat-field correction were performed. Data were taken in two-step dithered positions to enhance spatial sampling and cosmic rays removal by using the task **crrej** in the STSDAS package of IRAF. The journal of observations is summarized in Table 1. The processed F606W and F656N (H α) images with a total exposure time of 565 s and 1120 s are shown in Figures 1 and 2.

2.2 *HST* near-infrared imaging

High-resolution near-infrared images of IRAS 21282 were obtained by the Near-Infrared Camera Multiob-

ject Spectrometer (NICMOS) on *HST* through the observation program 7365 (PI: W. B. Latter). The data were all obtained on 1997 September 21. Two broad-band filters F160W ($\lambda_c = 15,931$ Å, $\Delta\lambda = 4,030$ Å) and F205W ($\lambda_c = 20,406$ Å, $\Delta\lambda = 6,125$ Å) were employed for these images. The 1.6 μ m (F160W) observations were made with Camera 1 (NIC1), which has a FOV of $11'' \times 11''$ with a spatial resolution of $0.''043$ pixel⁻¹. Another observation (F205W) was carried out with Camera 2 (NIC2), which provides a $19.''2 \times 19.''2$ FOV at a pixel scale of $0.''075$ pixel⁻¹. The total exposure times for these two observations (F160W and F205W) are both 384 s. The data were reduced and calibrated by the standard *HST* NICMOS pipeline. Standard flat-field correction and bias subtraction were performed. The multiple images of each band were combined together using the **calnicB** task in the STSDAS package of IRAF. A summary of NICMOS observations is also given in Table 1.

2.3 Optical spectroscopy

Optical mid-resolution spectra of the nebula were performed on the night of 2011 September 26 with the 2.16 m Telescope on the Xing-Long station of the National Astronomy Observatories of China (NAOC). An Optomechanics Research Inc. (OMR) spectrograph and a PI 1340×400 CCD were used, which result in a two-pixel resolution of ~ 2.0 Å. The spectral coverage of the observations is from 6300 to 7600 Å. To allow greater throughput for the weak emissions of faint nebula observed on this run, a slit width of $3.''0$ was set through bright core of the source along the north-south (NS) direction. The diaphragm sizes of the slit can cover most parts of this object. The exposure times ranged from 1200 to 6900 s, resulting in signal-to-noise ratios (S/N) of > 80 . The seeing conditions during the observing run varied between $2.''2$ and $2.''8$. Exposures of He-Ar arcs were obtained right before and after each

Table 2 Summary of optical spectral observation of IRAS 21282+5050

Observation Date	Wavelength Range (Å)	Resolution (Å pixel ⁻¹)	Width of Slit (arcsec)	Integration Time (s)
2011 Sep 26	6300 - 7600	1.0	3.0	2100 × 2
2011 Sep 26	6300 - 7600	1.0	3.0	1500
2011 Sep 26	6300 - 7600	1.0	3.0	1200

stellar spectrum and used for the wavelength calibration.

Data were reduced following standard procedures in the NOAO IRAF V2.16 software package. The CCD reductions included bias and flat-field correction, successful background subtraction and cosmic-ray removal. Flux calibration was derived from observations of at least three of the KPNO standard stars per night. The atmospheric extinction was corrected by the mean extinction coefficients measured for Xing-Long station, where the 2.16 m Telescope is located. A final spectrum for the nebula was produced using the combined OMR observations to improve the S/N and a summary of the spectroscopic observations is given in Table 2.

3 Results

3.1 Multiple lobes

Our *HST* ACS broad V-band (F606W) image of IRAS 21282 (Figure 1) clearly shows that this nebula is extended along the N-S direction with a size of $\sim 8.''51 \times 6.''15$, which is slightly larger than the size of $6.''5 \times 4.''8$ measured from the first optical image observed at *Canada-France-Hawaii Telescope* (Kwok, Hrivnak, & Langill 1993). Three pairs of bipolar lobes (labeled as $a - a'$, $b - b'$, and $c - c'$) emanating from the center of this nebula can also be seen. At the center is an elliptical cylindrical shell (marked as g) along the approximate SSE-NNW direction (PA = $157^\circ \pm 5^\circ$). Another extended diffuse structure (labeled as “torus”) can also be seen along the E-W direction around the waist of this nebula.

The axes of these three pairs of lobes $a - a'$, $b - b'$, and $c - c'$ intersect approximately at the position of the central star seen in Figs. 2 and 3. The position angles (PAs) of these three bipolar lobes are measured to be PA = $139^\circ \pm 3^\circ$, $13^\circ \pm 2^\circ$, and $35^\circ \pm 3^\circ$ for lobes $a - a'$, $b - b'$, and $c - c'$, respectively, which are not perpendicular to each other. Sizes of the lobes are measured by fitting the ellipses to the image. These three bipolar lobes have similar projected sizes on the sky. The measured angular sizes of three pairs of lobes

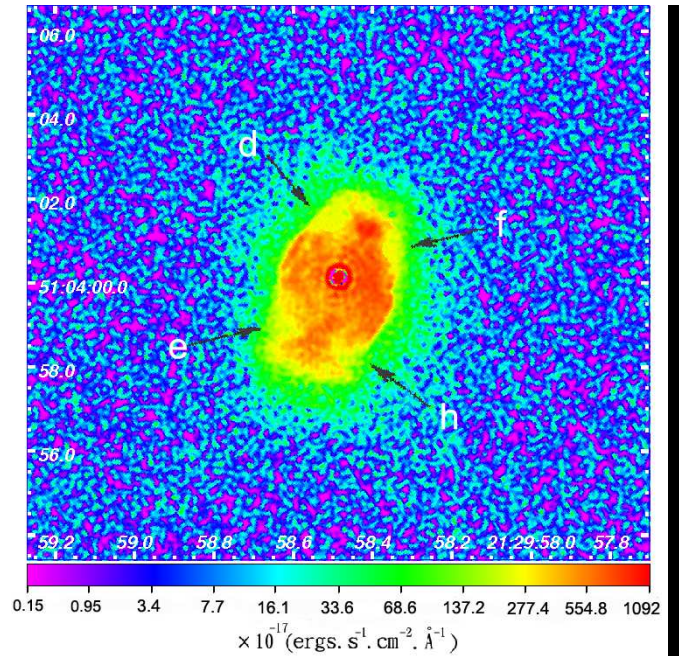


Fig. 2 *HST* WFPC2 $H\alpha$ image of IRAS 21282+5050. The main nebula seen in this $H\alpha$ image corresponds to the central cylindrical structure (marked as “ g ”) in Figure 1. Several low-density regions are marked as d , e , f , and h . North is up and east is to the left. The intensity display is on a logarithmic scale and the grey scale bar is given at the bottom in units of $\text{ergs cm}^{-2} \text{s}^{-1} \text{\AA}^{-1}$.

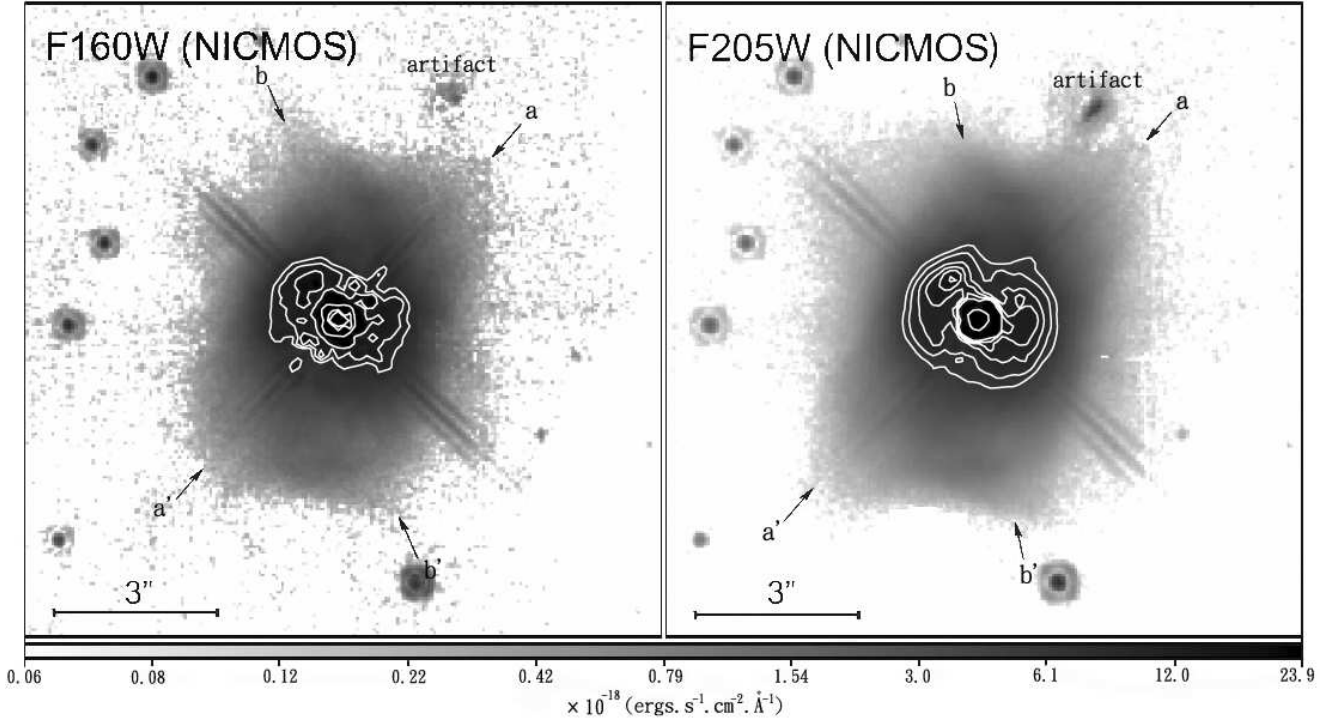


Fig. 3 *HST* NICMOS F160W (left) and F205W (right) images of IRAS 21282+5050. In the center is a bright torus (shown in logarithmic white line contours. The outer four contours are drawn at the 155, 200, 260, and 340 σ level above background sky brightness. The central compact contours indicate the position of the central star. Two pairs of bipolar lobes ($a-a'$ and $b-b'$) can be seen in both images, but the lobe $c-c'$ in Fig. 1 is not found in the NICMOS images. North is up and east is to the left. The intensity display is on a logarithmic scale and the grey scale bar is given at the bottom in units of $\text{ergs cm}^{-2} \text{ s}^{-1} \text{ \AA}^{-1}$.

($a - a'$, $b - b'$, and $c - c'$) are $9.''96 \times 2.''88$, $9.''02 \times 1.''64$, and $9.''66 \times 3.''04$.

Precise distances of PNs are extremely difficult to determine (see e.g., Stanghellini et al. 2017). Based on a comparison between the systematical velocity and the Galactic rotation, Likkell (1988) suggested that IRAS 21282 is close to the Sun with a distance of < 2 kpc. However, Shibata et al. (1989) found that in order to reach good agreement between the kinematical age of gas and the evolutionary age of the central star, one has to assume a distance of 2 kpc. A larger distance value of 3.38 kpc was derived from the four IRAS band fluxes, assuming a total infrared luminosity of $8,500 L_{\odot}$ for compact PNs (Casassus et al. 2001). The recent data release (DR) of Gaia trigonometric parallaxes of a large sample of PNs has allowed the derivation of model-independent distances for more PNs. Stanghellini et al. (2017) and Kimeswenger & Barría (2018) presented the distances of PNs in Gaia DR1 and DR2, respectively. The parallax of IRAS 21282+5050 was published in Gaia DR2. However, Bailer-Jones et al. (2018) argued that reliable distance cannot be obtained by inverting the parallax. Instead, they obtained distance scales by using a weak distance prior according to Galactic model, suggesting a distance of $3.57^{+0.26}_{-0.22}$ kpc for IRAS 21282+5050. This more reliable distance allows us to evaluate distance-dependent parameters of this PN with higher accuracy.

Adopting the distance of 3.57 kpc for IRAS 21282 (Bailer-Jones et al. 2018), the physical size of the total extent of lobe $a - a'$ is $\sim 0.17 \text{ sec}\theta \text{ pc}$, where θ is the inclination angle. Assuming the expansion velocity of 50 km s^{-1} (Cohen & Jones 1987), we derive a kinematic age of $\sim 3400 \text{ sec}\theta \text{ yr}$. This is consistent with the earlier suggestion that IRAS 21282 is a very young PN (Kwok, Hrivnak, & Langill 1993).

The WFPC $H\alpha$ image (Figure 2) shows an elliptical cylinder shell surrounding a bright central star. This shell corresponds to the cylinder-shaped structure labeled g in Figure 1. This elliptical cylinder structure has an angular size of $4.''92 \times 3.''01$. The major axis of the structure is oriented at $\text{PA} = 159^{\circ} \pm 3^{\circ}$, which is different from the axis of the lobe $a - a'$. The nebula shows an edge with high density contrast as well as several clumpy regions (Figure 2). It is possible that these regions are the results of projection of interlaced multiple lobes and/or ionized non-uniform dense nebula emitted by the central star. Several low-density regions (d, e, f, h) associated with the lobes $a - a'$ and $c - c'$ are also found. The multiple lobes seen in IRAS 21282 may represent the directions where the UV photons are escaping.

3.2 Dust torus

The two broad-band near-infrared F160W and F205W images (Fig. 3) have similar appearances. The counterparts of bipolar pairs $a - a'$ and $b - b'$ can be seen in Figure 3, but the $c - c'$ bipolar lobe is not. The central region of the nebula shows an elliptically shaped structure of size $\sim 6.''11 \times 4.''13$ with two prominent peaks along the ENE-WSW direction. The symmetry axis of the infrared nebula lies at the PA of $155^{\circ} \pm 2^{\circ}$, which is almost the same orientation as the elliptical shell structure observed in the $H\alpha$ image (see Section 3.1). The nebula is therefore likely to be an infrared counterpart of the $H\alpha$ cylinder-shaped shell. These two bright peaks (separated by $1.''65$) lie along an axis with $\text{PA} = 63^{\circ} \pm 3^{\circ}$, which is perpendicular to the major axis (polar direction) of the nebula.

If the double-peaked structure seen in the F160W and F205W images represent an oblique torus, then the emission from these two peaks could be the result of projection of a toroid viewed edge-on, implying that the elliptical nebula is oriented close to the plane of the sky. Such toroidal structures can be found in the PNs with binary nuclei (e.g., NGC 2346, Su et al. 2004) and (M2-9, Castro-Carrizo et al. 2010), and has been interpreted as the result of sweeping up previously-ejected AGB circumstellar materials by a later developed fast, collimated wind (Mastrodemos & Morris 1998).

This torus is not obvious in the $H\alpha$ image, probably because the dust torus is optically thick to the UV photons and the this structure is not ionized. The near-infrared morphology of IRAS 21282 (Figure 3) seems to be consistent with that at H-band (Cheng 2005), $2.2 \mu\text{m}$ (Meixner et al. 1993), and H_2 images (Davis et al. 2005), all of which show a central peak, probably the result of diffuse scattering light from the central star or as the result of the low resolution of these images. Further comparisons between our *HST NICMOS* observations with the deconvolved infrared images at 3.3, 8.5, 10.0, 11.3, and $12.5 \mu\text{m}$ of Meixner et al. (1993) and Keck ones at K-continuum, L' , M_s , and PAH bands of Cheng (2005) show that the elongation direction of this nebula and the locations of two bright peaks are very similar, which indicates that the infrared emission in these images are mainly dominated by the same dust continuum or some contributions from UIE bands (Meixner et al. 1993). The dust component heated by the starlight escapes more directly through the polar direction. The presence of dust torus in IRAS 21282 also suggests that the mass of the waist part is much larger than that of its poles.

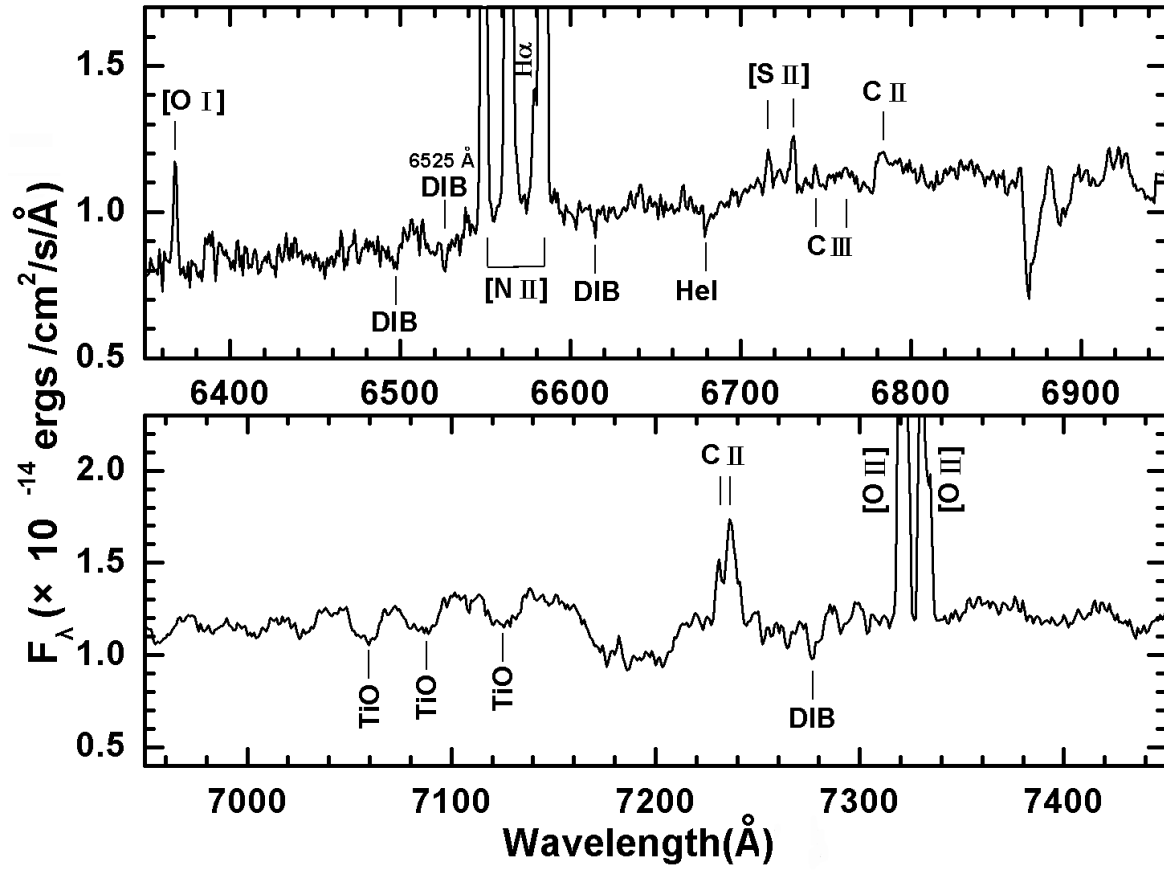


Fig. 4 NAOC OMR spectrum of IRAS 21282+5050 (not corrected for extinction) in wavelength range of 6350 Å to 7450 Å. The emission lines, DIBs, and absorption lines are marked.

Table 3 Atomic lines in IRAS 21282+5050

λ_{obs} (Å)	Identification		Observed Flux ^a	Dereddened Flux ^a	RV ^b (km s ⁻¹)
	λ_{lab} (Å)	Ion			
Emissions					
6364.12	6363.78	[OI]	1.25(23.2)	1.50(23.2)	16 ± 6
6549.15	6548.10	[NII]	38.42(1.4)	38.94(1.4)	48 ± 3
6563.75	6562.77	H α	100.00(0.9)	100.00(0.9)	45 ± 2
6577.55 ^c	6578.03	CII	0.40(50.5)	0.39(50.9)	-22 ± 11
6584.20	6583.50	[NII]	125.00(2.5)	122.68(2.5)	32 ± 3
6716.65	6716.40	[SII]	0.80(19.6)	0.70(19.6)	11 ± 12
6722.21	6721.35	[OII]	0.30(58.4)	0.26(58.4)	38 ± 19
6730.91	6730.82	[SII]	1.11(12.7)	0.96(12.7)	4 ± 9
6743.93	6744.40	CIII	0.05(36.1)	0.04(36.1)	-21 ± 12
6761.42	6762.20	CIII	0.04(48.4)	0.04(48.5)	-35 ± 18
6779.66 ^d	6779.90	CII	0.53(6.8)	0.44(6.8)	-11 ± 8
6782.74 ^d	6783.90	CII	0.22(19.1)	0.18(19.1)	-51 ± 19
6798.28	6798.10	CII	0.50(43.2)	0.41(43.2)	8 ± 15
7230.48	7231.30	CII	0.90(11.8)	0.52(11.8)	-34 ± 6
7236.45	7236.40	CII	1.41(9.8)	0.81(9.9)	2 ± 5
7321.15	7319.99	[OII]	24.47(10.9)	13.19(10.9)	48 ± 5
7331.98	7330.73	[OII]	19.33(17.1)	10.34(17.1)	51 ± 5
Photospheric absorption from hot star					
6678.84	6678.15	HeI	31 ± 22

^aThe line fluxes were normalized to F(H α)=100 and percentage uncertain errors of the flux measurements are given within brackets.^bError measured using the method described in Manick et al. (2015).^cOriginated from the companion star.^dFrom Gaussian fitting routine of closed lines.

3.3 Optical spectroscopy

Although optical spectra with different resolutions of this nebula have been presented by Cohen & Jones (1987) and Leuenhagen & Hamann (1998), their studies focused on the spectral type of central star, velocity distributions of lines, and element abundances of nitrogen, neon, and silicon of the nebula. We have performed new spectroscopic observations and the results are shown in Figure 4. The spectrum of IRAS 21282 is dominated by prominent emission lines of [NII] $\lambda\lambda 6548, 6584$, H α , [SII] $\lambda\lambda 6717, 6731$, and [OII] $\lambda\lambda 7319, 7330$. Some weak emission features such as CII $\lambda\lambda 6578, 6779, 6784, 6798, 7231, 7236$ and CIII $\lambda\lambda 6744, 6762$ can also be seen. The CII/CIII emission ratio suggests that the nebula is carbon-rich with a cool [WC 11] nucleus (Cohen & Jones 1987; van der Hucht et al. 1981). From the flatness of the quotient spectrum through IRAS 21282 divided by a reddened O7- type star (see Figure 3, Cohen & Jones 1987), an extinction coefficient value of $A_v = 5.8$ mag was derived. This implies an E(B-V) value of 1.88, which can be attributed mostly to the circumstellar extinction.

The emission line fluxes and their radial velocities (RVs) measured from the spectrum are listed in Table 3. The measured central wavelengths of the emissions and line identifications are listed in Columns 1 - 3. Column 4 and 5 give the observed and dereddened fluxes (normalized to H $\alpha = 100$) measured using the Gaussian fitting routine for this nebula. The RVs of the line features measured from our observation are given in Column 6. Although the H α line measurements are affected by central-star absorption, the flux uncertainties due to the effect are relatively minor. The raw integrated H α flux measured from main nebula for this object is 3.24×10^{-13} erg cm $^{-2}$ s $^{-1}$. The characteristic uncertainty of flux measurements is about 24%. The line ratio of [NII] $\lambda\lambda 6584/\lambda\lambda 6548$ of IRAS 21282 is 3.2, in good agreement with the theoretical predictions. Using the [SII] $\lambda\lambda 6731/\lambda\lambda 6717$ line ratio and assuming an electron temperature $T_e = 10,000$ K, we derive the electron density $n_e = 1900$ cm $^{-3}$ for the nebula, which is consistent with the previously reported range of $2,000 - 10^4$ cm $^{-3}$ (Likkell et al. 1994) and $200 - 10^5$ cm $^{-3}$ (Cohen & Jones 1987).

3.3.1 Circumstellar diffuse interstellar bands

One of the unique aspect of IRAS 21282 is the presence of circumstellar diffuse interstellar bands (DIB). Previously, DIBs at $\lambda\lambda 5780, 5797, 6177, 6203, 6270$, and 6613 Å have been detected by Cohen & Jones (1987) and Le Bertre & Lequeux (1992). In Figure 4, we show

the detections of DIBs at $\lambda\lambda 6498, 6613$, and 7276 Å. In addition, a new DIB band at 6525 Å (first discovered in PN Tc 1, García-Hernández & Díaz-Luis 2013) is also detected in our spectrum. This feature may be related to larger fullerenes (e.g., C $_{80}$, C $_{240}$, C $_{320}$, and C $_{540}$) and buckyonions in the circumstellar envelope.

3.3.2 A cool companion

Interestingly, molecular TiO absorptions at $\lambda\lambda 7054, 7088, 7126$ Å characteristic of late-type stars can be seen in the spectrum. These TiO absorption bands suggest the presence of a cool companion to the exciting source of this nebula, raising the possibility that there may be a binary nucleus in IRAS 21282 (Cohen & Jones 1987; Meixner et al. 1993).

4 Spectral energy distribution

Young PNs often show strong infrared excess due to thermal emission of dust components and a significant fraction of their total energy output is emitted in the infrared (Zhang & Kwok 1991). In order to determine the relative contributions of the photospheric, nebular gas, and dust components to the total observed fluxes for young PNs, we have constructed spectral energy distributions (SEDs) for IRAS 21282 (Figure 5). The optical U, B, V, and R photometry of central star of IRAS 21282 are obtained from Cohen & Jones (1987). Near-infrared photometry at I, L', M, J, H, and K bands from ground-based and *Two Micron All Sky Survey* (2MASS) observations are taken from Kwok, Hrivnak, & Langill (1993) and 2MASS database, respectively. In the mid-infrared, data from *Midcourse Space Experiment* (MSX), *IRAS*, and *AKARI* Point Source Catalogues are used. We have also added photometric measurements derived from the infrared images from *Wide-field Infrared Survey Explorer* (WISE; Wright et al. 2010) survey. Also plotted on Figure 5 are the *Infrared Space Observatory* (ISO) SWS and LWS observations of the object. Summaries of the photometric and spectroscopic data used are given in Tables 4 and 5, respectively¹.

4.1 Total flux emitted by IRAS 21282

We can see from the SED that most of the flux from IRAS 21282 is emitted in the mid-infrared. If we take

¹We note that some filters are broad and color corrections may be needed for some flux densities given in Figure 5 and Table 4. The color correction factors for the *WISE* bands can be found in Wright et al. (2010)

Table 4 Photometric measurements of IRAS 21282+5050

Filters	Flux/Flux density	Reference
Central star and nebula		
U (mag)	16.33	Cohen & Jones (1987)
B (mag)	15.98	Cohen & Jones (1987)
V (mag)	14.40	Cohen & Jones (1987)
R (mag)	13.39	Cohen & Jones (1987)
I (mag)	12.57±0.02	Kwok, Hrivnak, & Langill (1993)
Dust		
L' (mag)	6.59±0.02	Kwok, Hrivnak, & Langill (1993)
M (mag)	5.80±0.04	Kwok, Hrivnak, & Langill (1993)
2MASS J (mag)	11.504±0.019	Cutri et al. (2003)
2MASS H (mag)	10.709±0.017	Cutri et al. (2003)
2MASS Ks (mag)	9.591±0.020	Cutri et al. (2003)
WISE F 3.4 μm (Jy)	0.61±0.02	Cutri et al. (2012)
WISE F 4.6 μm (Jy)	0.94±0.02	Cutri et al. (2012)
WISE F 12 μm (Jy)	77.95±1.46	Cutri et al. (2012)
WISE F 22 μm (Jy)	62.10±0.10	Cutri et al. (2012)
MSX F 8.3 μm (Jy)	24.58±1.01	Egan et al. (2003)
MSX F 12.1 μm (Jy)	62.05±3.10	Egan et al. (2003)
MSX F 14.7 μm (Jy)	67.08±4.11	Egan et al. (2003)
MSX F 21.3 μm (Jy)	61.79±3.71	Egan et al. (2003)
IRAS F 12 μm (Jy)	50.54±1.77	Moshir et al. (1992)
IRAS F 25 μm (Jy)	72.82±2.99	Moshir et al. (1992)
IRAS F 60 μm (Jy)	31.88±1.28	Moshir et al. (1992)
IRAS F 100 μm^a (Jy)	31.81±2.99	Moshir et al. (1992)
AKARI F 9 μm (Jy)	26.51±0.09	Ishihara et al. (2010)
AKARI F 18 μm (Jy)	64.05±0.47	Ishihara et al. (2010)
AKARI F 65 μm (Jy)	25.73±1.10	Ishihara et al. (2010)
AKARI F 90 μm (Jy)	19.62±0.77	Ishihara et al. (2010)
AKARI F 140 μm (Jy)	5.03±0.51	Ishihara et al. (2010)
AKARI F 160 μm^b (Jy)	3.71±2.71	Ishihara et al. (2010)
Free-free emission		
IRAM F 1300 μm (mJy)	5.40±1.20	Castro-Carrizo et al. (2010)
IRAM F 2600 μm (mJy)	2.90±0.60	Castro-Carrizo et al. (2010)
15 GHz (mJy)	6.80±1.02	Likkel et al. (1994)
8.4 GHz (mJy)	4.28±0.04	Knapp et al. (1995)
5 GHz (mJy)	6.90±0.69	Likkel et al. (1994)
5 GHz (mJy)	8.00±0.80	Meixner et al. (1993)

^aNote that the flux measured from 100 μm is an upper limit.^bFrom AKARI database. Note that the 160 μm flux is uncertain.

Table 5 *ISO* observations of IRAS 21282

PN	Name	Instrument	Observation Date	Wavelength Range	Exposures
SWS Spectra					
G 093.9-00.1	IRAS 21282+5050	TDT 05602477	1996 Jan 12	2.4 - 45.2 μm	1860 s
		TDT 15901777	1996 Apr 24	2.4 - 45.2 μm	3462 s
		TDT 36801940	1996 Nov 18	2.4 - 45.2 μm	1913 s
LWS Spectra					
G 093.9-00.1	IRAS 21282+5050	TDT 36801941	1996 Nov 18	43 - 186.5 μm	1004 s
		TDT 34602320	1996 Oct 28	43 - 195.8 μm	1268 s

the peak flux (λF_λ) of the SED as $\sim 10^{-8} \text{ erg cm}^{-2} \text{ s}^{-1}$ and assume that this is the peak of a blackbody, then the total emitted flux is approximately $(\lambda F_\lambda)_{\text{peak}}/0.736 = 1.4 \times 10^{-8} \text{ erg cm}^{-2} \text{ s}^{-1}$ (Kwok 2007, p. 521). Assuming a distance of 3.57 kpc, the total luminosity emitted by the object is $5600 L_\odot$. Since the observed SED is broader than a single-temperature blackbody, this value should be a minimum. If we plot the SED in units of F_λ and sum up the area under the curve of the SED, the total flux is $1.6 \times 10^{-8} \text{ erg cm}^{-2} \text{ s}^{-1}$, giving a luminosity of $\sim 6400 L_\odot$.

4.2 Evidence for a cool companion

The observed optical fluxes represent the sum of the reddened photospheric emission from the central star and nebular emissions. The gaseous nebular continuum is the sum of the bound-free ($b-f$), free-free ($f-f$), and two-photon emissions. We use the emission coefficients given in Kwok (2007) at a typical electron temperature $T_e = 10^4 \text{ K}$. At wavelengths longward of $\lambda \geq 2 \text{ mm}$, $f-f$ emission dominates over dust emission. The emission measure of the nebular gas component can therefore be constrained by the observed $f-f$ fluxes in the radio.

From the SED, we note that the observed *WISE* $3.4 \mu\text{m}$ and L' -band fluxes are higher than the expected near-infrared continuum. These excesses could be due to contribution from the $3.3 \mu\text{m}$ UIE band (Meixner et al. 1993; Hora, Latter, & Deutsch 1999). UIE bands at 6.2, 7.7-7.9, 8.6, 11.3, 12.7, and $14.2 \mu\text{m}$ and a weak band at $6.0 \mu\text{m}$ be seen in the *ISO* spectrum (Hsia et al. 2016).

The near-infrared continuum of the object cannot be fitted by the nebular gas component alone and must contain contributions from photospheric and/or hot dust components. In order to fit the optical and near infrared parts of the SED, we need two central stars of temperatures of 6,000 K and 25,000 K. Assuming a distance of 3.57 kpc, the respective luminosities of the two central stars are 1,900 and 5,400 L_\odot . The total luminosity of the object (7,300 L_\odot) is higher than the earlier estimate of 6,400 L_\odot because part of the radiation from the central star in the UV is not represented

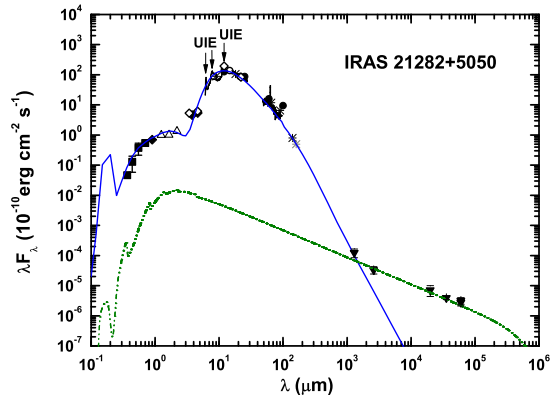


Fig. 5 SED of IRAS 21282+5050 in the wavelength range from 0.1 μm to 1 m. The U, B, V and R photometry are shown as filled squares, the I, L' and M near-IR photometry as filled diamonds, the 2MASS photometry as open triangles, *WISE* photometry as open diamonds, *MSX* as open circles, *IRAS* as filled circles, and *AKARI* photometry as asterisks. The light asterisk represents the uncertain *AKARI* detection. The *IRAS* 100 μm flux is an upper limit. The *ISO* SWS and LWS spectra are also plotted. The green curve represents the nebular gas $b-f$ and $f-f$ emissions. The blue curve is a dust continuum radiation transfer model (DUSTY (Ivezic, Nenkova, & Elitzur 1999)) fit of the emergent flux. The excess in the ultraviolet part of the model curve is the reddened photosphere of the hot central star.

in the total observed fluxes. The near infrared (from 0.8 to 5 μm) emission from IRAS 21282 are due to the cool companion as well as emission from the dust torus. Most of the infrared flux ($\lambda > 5\mu\text{m}$) must originate from a much larger cool dust envelope extending far beyond the optical nebula.

5 3-D model simulations

From the results presented in Section 3.1, and 3.2, we suggest that IRAS 21282 is a young multipolar PN. In order to visualize its intrinsic structures, we have constructed a 3-D modeling using the software package *SHAPE*² (Steffen et al. 2011), which is a morphokinematic modeling tool used to analyze the 3-D structures of gaseous nebulae. A 3-D multi-component model is constructed and the integrated emission intensities ($\int n_e^2 d\ell$) along the line of sight are compared with the observed surface brightness distribution in the *HST* images.

Our model of IRAS 21282 consists of five major components: four pairs of bipolar lobes and an equatorial dust torus. The observed three pairs of bipolar lobes ($a-a'$, $b-b'$, and $c-c'$) are directly incorporated in the model. We also create another small pair of lobes with openings at the tips that is aligned along the plane of the sky. This pair of ionized bipolar lobes is identified as a distinct component since it can be seen in the $\text{H}\alpha$ image (Figure 2), whereas the outer three lobes are only visible in the F606W broad-band image (Figure 1). The inner bipolar component with a shell-like appearance is referred to as lobe g in Figure 1 (see Section 3.1). Assuming that the lengths of these three pairs of lobes are equal and lobe $a-a'$ is perpendicular to the line of sight (at inclination angle $\theta = 0^\circ$ relative to the plane of the sky), we derive the inclination angles of lobes $b-b'$ and $c-c'$ to be -25° and -14° , respectively.

In addition, we also include a toroidal structure as the counterpart of infrared torus seen in the *HST NICMOS* images. The center of this dust torus is set to the intersection of the four pairs of bipolar lobes. The orientation of dust torus is fitted to the locations of two bright peaks, which have a separation distance of about $1.''16$. According to the spectroscopic measurements at H_2 2.12 μm (Davis et al. 2005) and our previous results, the inclination angle of observed torus is assumed to be 0° (viewed edge-on). In our model, the bipolar lobe g is viewed side-on and its symmetry axis is perpendicular to the dust torus. After an inspection of the F606W and NICMOS images, three outer bipolar lobes

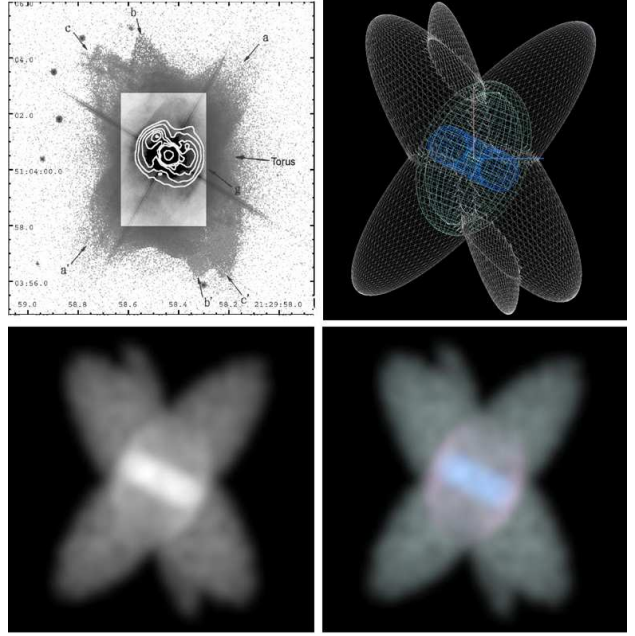


Fig. 6 Comparison of optical-infrared observations and the corresponding 3-D model images of IRAS 21282+5050. Upper left: *HST/ACS* F606W image (grey scale) is overlaid with the *NICMOS* F205W image (shown as white-line logarithmic contours). The outer four contours drawn are the same as the plotting in Figure 3. Upper right: *SHAPE* 3-D mesh model. The bipolar lobes $a-a'$, $b-b'$, and $c-c'$ are displayed in white and the fourth pair of lobes observed in the *HST* $\text{H}\alpha$ image (marked as g in Figure 1) is shown in light blue. The infrared torus observed in *HST NICMOS* image is shown in dark blue. Lower left: the rendered image in grey scale. Lower right: rendered image with the outer three lobes ($a-a'$, $b-b'$, and $c-c'$), inner bipolar lobe, and the equatorial torus shown in white, red, and blue, respectively. A Gaussian blur has been applied to the renderings to simulate the telescope beam.

²<http://www.astrosen.unam.mx/shape/>

($a - a'$, $b - b'$, and $c - c'$) and the dust torus of the nebula show no shell-like structure, these components are given a uniform density distribution. For the fourth pair of lobe seen in the $H\alpha$ image (assumed to correspond to “ g ” in Figure 1), the central element has a bipolar shell structure and is assumed to be identical. The observed and model parameters of these structures are listed in Table 6.

A comparison of the *HST* optical-infrared observations and corresponding model images are shown in Figure 6, in which the model intensity distributions are convolved with a Gaussian to simulate the telescope beam. As we can see from the rendered images in Figure 6 (lower panels), our modeling gives a good approximation to observed images of IRAS 21282 and some basic observed features can be reasonably reproduced by SHAPE model.

Our model not only helps us to visualize the intrinsic 3-D structures of IRAS 21282 but can also predict what this object may look like when viewed from different orientations. In Figure 7, we show a comparison of the projected model images of IRAS 21282 viewed from different angles and compare these results to the images of two other young multipolar PNs (IC 5117 and NGC 6790). From Figure 7, we note that the rendered images of IRAS 21282 differ from those of IC 5117 and NGC 6790. The bipolar lobes of IC 5117 and NGC 6790 show shell-like structures, they are modeled using identical bipolar shells, whereas the three pairs of bipolar lobes are constructed using a uniform density distribution for IRAS 21282. When the model is rotated to the right and next rotated 90° counterclockwise, the three pairs of lobes appear closer together and the nebula resembles a central elliptical shell. The appearance of rotated model is similar to the young PN IC 5117 (Hsia et al. 2014). When the model is viewed from the bottom (pole-on), the object shows two pairs of distinct lobes and a bright ring, similar to the apparent structures of NGC 6790 (Hsia et al. 2014) and NGC 6644 (Hsia et al. 2010). This suggests that one single multipolar structure may have different apparent morphologies when viewed from different orientations. The statement that “each multipolar PN is unique” is therefore unlikely to be true as different 2-D morphologies may originate from the similar intrinsic 3-D structures (Chong et al. 2012).

In the present exercise, we try to construct a 3-D model from its corresponding 2-D images, but the presented model just provides a possible morphological solution for the PN IRAS 21282. We should note that because of projection effects, it is possible that different 3-D models can lead to the images with a similar appearance. Only position-velocity (PV) diagrams obtained from spectroscopic observation can break this

degeneracy. Further observations with integral field spectroscopy on large optical telescopes are needed to constraint our model.

6 Comparison with other multipolar planetary nebulae

When stars evolve from AGB to PN stages, some develop hydrogen-deficient atmospheres above their C-O electron-degenerate cores. But the exact mechanism removing hydrogen is still an open issue. The spectra of these objects always mimics the massive Wolf-Rayet (WR) star exhibiting strong stellar wind with mass-loss rate up to about $10^{-6} M_\odot \text{ yr}^{-1}$ (Crowther 2008). Based on the strengths of emission lines, the visual spectral classification of [WR]-type central star of PN (CSPN) can be classified as [WC] (carbon-rich), [WN] (nitrogen-rich), and [WO] (oxygen-rich) subtypes (Crowther 2008). The hydrogen atmosphere could be removed at (i) at the end of the AGB stage (AGB final thermal pulse; Herwig 2001); (ii) at the post-AGB stage (late thermal pulse; Blocker 2001); or (iii) at white dwarf cooling track (very late thermal pulse; Lawlor & MacDonald 2002). An hypothesis for the origin of [WR]-type central stars is by binary/planet interaction (De Marco & Soker 2002; De Marco 2008), where a companion or a massive planet is engulfed by an AGB star.

IRAS 21282 has been identified as a multipolar PN with the cool [WC 11] nucleus (see Section 3.3). It would be interesting to investigate whether the multipolar structures are related to the [WR] nature of the central star. For that purpose, we collected a sample of twenty-three known multipolar PNs that has been studied in previous literatures (Clark et al. 2013; Danehkar & Parker 2015; Guerrero & Manchado 1998; Guerrero et al. 2013; Guillén et al. 2013; Hsia et al. 2010, 2014; López et al. 1998, 2012; Manchado, Stanghellini, & Guerrero 1996; Sabin et al. 2012; Sahai 2000; Vázquez et al. 2008). The adopted physical parameters of these sources are listed in Table 7. The columns 1 and 2 give the PNG numbers and object names. The spectral types of central sources and binarity of them are given in columns 3 and 4.

From Table 7, we find that that a significant fraction ($\sim 44\%$) of multipolar PNs in our sample shows [WR]-type nucleus and 4 objects (M 1-30, M 1-61, NGC 6309, and NGC 6644) have [WEL]-type central stars. Possible explanations to such correlations include multiple lobes produced by strong turbulence blowing from [WC]-type central stars (e.g. Acker et al. 2002; Gesicki et al. 2003) or atmospheric instabilities in the shells during the AGB stages (Steffen et al. 2013).

Table 6 Comparison of observed and model parameters of the lobes and torus

Parameters	Observed			Model		
	Position angle ^a (°)	Size ^b ($''$)	Inclination angle ^c (°)	Position angle ^a (°)	Size ^b ($''$)	Inclination angle ^c (°)
Lobe $a - a'$	139 ± 3	9.96×2.88	...	139	9.96×2.88	0
Lobe $b - b'$	13 ± 2	9.02×1.64	...	13	9.96×1.64	-25
Lobe $c - c'$	35 ± 3	9.66×3.04	...	35	9.96×3.04	-14
Lobe g	157 ± 5	4.92×3.01	0^d	157	4.48×3.01	0
Dust torus	63 ± 3^e	1.65^f	90^g	63	1.65^f	90

^aMeasured from the major axis orientation.

^bMeasured by fitting the ellipses to the image.

^cAssuming the orientation angle of sky plane is 0° .

^dFrom Davis et al. (2005).

^eDerived from peak position of torus.

^fPeak separation of torus.

^gFrom Davis et al. (2005).

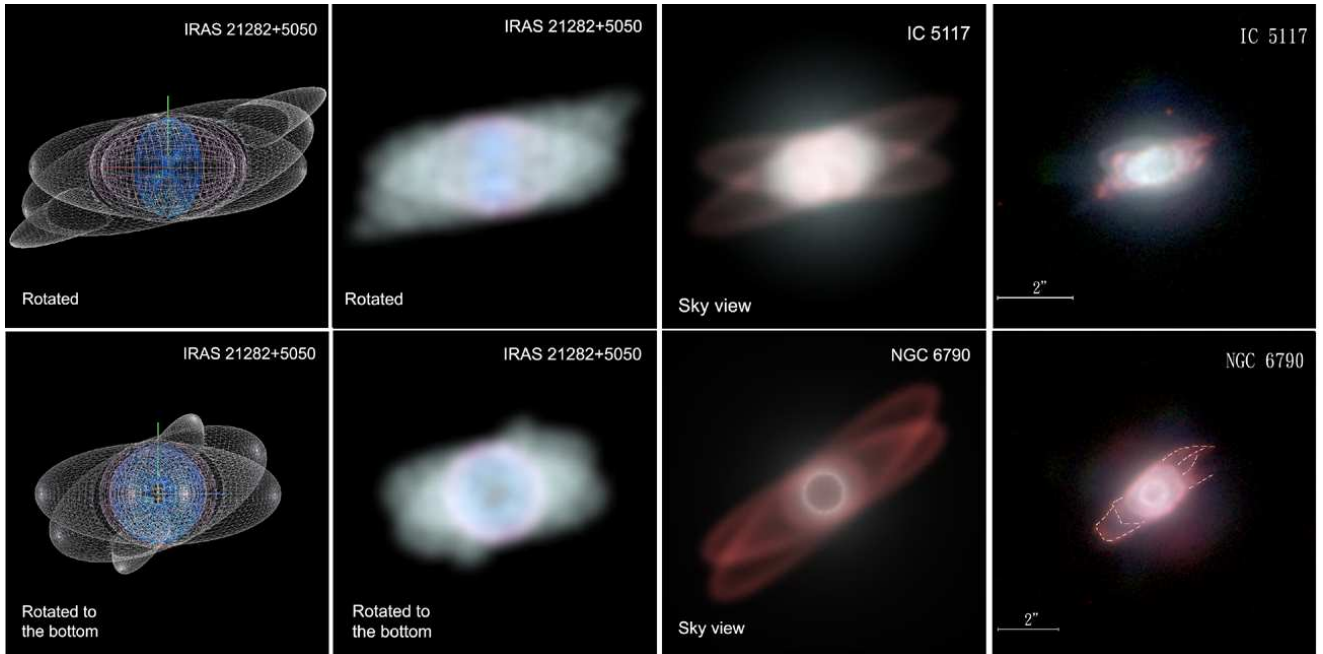


Fig. 7 Comparison of the model renderings of IRAS 21282 at different orientations and the model and observed images of multipolar PNs IC 5117 and NGC 6790. Upper panels, from left to right: (1) 3-D mesh image of IRAS 21282 rotated to the right and 90° counterclockwise; (2) the corresponding rendered image; (3) the rendered image of PN IC 5117; and (4) a composite-color *HST* image of IC 5117. Lower panels, from left to right: (1) 3-D mesh image of IRAS 21282 viewed from the bottom (near pole-on); (2) the corresponding rendered image; (3) the rendered image of PN NGC 6790; and (4) composite-color *HST* narrow-band image of NGC 6790. The *HST* and their corresponding rendered images of IC 5117 and NGC 6790 are taken from Hsia et al. (2014).

Table 7 Properties of studied multipolar and quadrupolar planetary nebulae

PN G	Name	Spectral type [‡]	Binarity
002.6-03.4	M 1-37	[WC 11] ^a	No ^b
008.3-07.3	NGC 6644	[WEL] ^a	Possible ^c
009.6+14.8	NGC 6309	[WEL] ^a	–
019.4-05.3	M 1-61	[WEL] ^a	–
021.8-00.4	M 3-28	–	Possible ^d
024.8-02.7	M 2-46	–	–
037.8-06.3	NGC 6790	[WN] ^a	–
043.0-03.0	M 4-14	–	Possible ^d
048.7+02.3	K 3-24	–	Possible ^d
064.6+48.2	NGC 6058	O9 ^a	–
068.8-00.0	M 1-75	–	Possible ^e
074.5+02.1	NGC 6881	–	Possible ^f
084.7-08.0	Kn 26	–	Possible ^g
089.0+00.3	NGC 7026	[WO 3] ^a	–
089.8-05.1	IC 5117	[WR] ^a	–
093.9-00.1	IRAS 21282	[WC 11] ^a	Possible ^{h,i}
234.8+02.4	NGC 2440	–	–
285.6-02.7	Hen 2-47	[WC 10-11] ^a	–
300.7-02.0	Hen 2-86	[WC 4] ^a	–
307.2-03.4	NGC 5189	[WO 1] ^a	Yes ^j
309.1-04.3	NGC 5315	[WO 4] ^a	Possible ^j
321.0+03.9	Hen 2-113	[WC 10] ^a	No ^j
332.9-09.9	Hen 3-1333	[WC 10] ^a	No ^j
355.9-04.2	M 1-30	[WEL] ^a	–
359.3-00.9	Hb 5	–	–

^aWeidmann & Gamen (2011)^bLutz et al. (2010)^cHsia et al. (2010)^dManchado et al. (1996)^eSantander-García et al. (2010)^fGuerrero & Manchado (1998)^gGuerrero et al. (2013)^hThis studyⁱCohen & Jones (1987)^jManick et al. (2015)

The possible presence of binary nuclei detected in multipolar PNs (Table 7) has led to suggestion that precessions of mass-losing star’s rotation axis and jets with time-dependent ejection from the binary or multiple sub-stellar companions in the nuclei could need to the formation of multipolar PNs (García-Segura 1997; Velázquez et al. 2012). It would be interesting to investigate further whether the binary nature of the central star of IRAS 21282 plays any role in the observed multipolar structure of this object.

7 Conclusions

From *HST* high-angular-resolution optical and near-infrared observations, we have identified at least three pairs of bipolar lobes outside the main elliptical shell in the PN IRAS 21282. In addition, we find an infrared torus which is approximately perpendicular to the elliptical shell. A cylindrical shape structure found in the optical image could represent a fourth pair of bipolar lobes with a symmetry axis perpendicular to the dust torus.

The optical spectrum of the central star exhibits TiO absorption bands. Different emission lines show different RVs, which can be roughly divided into two groups. These results suggest the presence of a cool companion. A number of circumstellar DIBs are seen in the optical spectrum. It would be interesting to investigate whether the presence of the DIBs are related to the circumstellar UIE bands.

In order to illustrate the 3-D intrinsic structures of IRAS 21282, we have constructed a model that allows the visualization of the PN viewed from different orientations. The simulated rotated images of this object show that IRAS 21282 may have similar intrinsic structures as other multipolar PNs, suggesting that each multipolar PN is not unique and multipolar structures are common among PNs.

A significant fraction ($\sim 44\%$) of multipolar PNs in our sample is found to have [WR]-type central stars. It would be interesting to explore whether the multi-nebular properties of these nebulae are related to the spectral properties of the central sources.

IRAS 21282 is another example of the growing list of multipolar PNs found as the result of higher sensitivity and dynamical range imaging. It is possible that the multipolar phenomenon is much more common than previously believed and multipolar nature of PNs may be a norm rather than an exception.

Acknowledgements We thank an anonymous referee for his/her helpful comments. Part of the data

presented in this paper were obtained from the Multi-mission Archive at the Space Telescope Science Institute (MAST). STScI is operated by the Association of Universities for Research in Astronomy, Inc., under NASA contract NAS5-26555. Support for MAST for non-HST data is provided by the NASA Office of Space Science via grant NAG5- 7584 and by other grants and contracts. We acknowledge the support of the staff of the Xinglong 2.16m telescope. This work was partially supported by the Open Project Program of the Key Laboratory of Optical Astronomy, National Astronomical Observatories, Chinese Academy of Sciences. The Laboratory for Space Research was established by a grant from the University Development Fund of the University of Hong Kong. Financial support for this work is supported by the grants from Science and Technology Development Fund of Macau (project codes: 119/2017/A3 and 061/2017/A2) and a grant to SK from the Natural and Engineering Research Council of Canada.

References

- Acker, A., Kesicki, K., Grosdidier, Y., & Durand, S. 2002, *Astron. Astrophys.*, 384, 628
- Bailer-Jones, C. A. L., Rybizki, J., Fouesneau, M., Man-telet, G., & Andrae, R., 2018, *Astron. J.*, 156, 58
- Balick, B. 1987, *Astron. J.*, 84, 671
- Blöcker, T. 2001, *Astrophys. Space Sci.*, 275, 1
- Casassus, S., Roche, P. F., Aitken, D. K., & Smith, C. H. 2001, *Mon. Not. R. Astron. Soc.*, 320, 424
- Castro-Carrizo, A., Quintana-Lacaci, G., Neri, R., et al. 2010, *Astron. Astrophys.*, 523, A59
- Cheng, J. 2005, High-Resolution Imaging of Objects in the Post-AGB to Planetary Nebula Transition,
- Chong, S.-N., Kwok, S., Imai, H., Tafoya, D., & Chibueze, J. 2012, *ApJ*, 760, 115
- Clark, D. M., López, J. A., Steffen, W., et al. 2013, *Astron. J.*, 145, 57
- Cohen, M., Tielens, A. G. G. M. & Allamandola, L. J. 1985, *Astrophys. J. Lett.*, 299, 93
- Cohen, M., & Jones, B. F. 1987, *Astrophys. J. Lett.*, 321, 151
- Crowther, P. A., 2008, in *Hydrogen-Deficient Stars*, ed. K. Werner, & T. Rauch, ASP Conf. Ser., 391, 83
- Cutri, R. M., et al. 2003, *VizieR Online Data Catalog: II/246*
- Cutri, R. M., Wright, E. L., Conrow, T. A. O. et al. 2012, *VizieR Online Data Catalog: II/311*
- Danehkar, A., & Parker, Q. A. 2015, *Mon. Not. R. Astron. Soc.*, 449, L56
- Davis, C. J., Smith, M. D., Gledhill, T. M., et al. 2005, *Mon. Not. R. Astron. Soc.*, 360, 104
- De Marco, O., 2008, in *Hydrogen-Deficient Stars*, ed. K. Werner, & T. Rauch, ASP Conf. Ser., 391, 209
- De Marco, O., & Soker, N. 2002, *Publ. Astron. Soc. Pac.*, 114, 602
- Egan, M. P., Price, S. D., Kraemer, K. E., et al. 2003, The Midcourse Space Experiment Point Source Catalog v2.3, Air Research Laboratory Technical Report AFRL-VS-TR- 2003-1589
- García-Segura, G. 1997, *Astrophys. J. Lett.*, 489, L189
- García-Segura, G. 2010, *Astron. Astrophys.*, 520, L5
- García-Hernández, D. A. & Díaz-Luis, J. J. 2013, *Astron. Astrophys.*, 550, 6
- Gesicki, K., Acker, A., & Zijlstra, A. A. 2003, *Astron. Astrophys.*, 400, 957
- Guerrero, M. A., & Manchado A. 1998, *Astrophys. J.*, 508, 262
- Guerrero, M. A., Miranda, L. F., Ramos-Larios, G., & Vázquez, R. 2013, *Astron. Astrophys.*, 551, 53
- Guillén, P. F., Vázquez, R., Miranda, L. F., et al. 2013, *Mon. Not. R. Astron. Soc.*, 432, 2676
- Herwig, F., 2001, *Astrophys. Space Sci.*, 275, 15
- Hora, J. L., Latter, W. B., & Deutsch, L. K. 1999, *Astrophys. J. Suppl. Ser.*, 124, 195
- Hrivnak, B. J., Geballe, T. R., & Kwok, S. 2007, *Astrophys. J.*, 662, 1059
- Hsia, C.-H., Kwok, S., Zhang, Y., et al. 2010, *Astrophys. J.*, 725, 173
- Hsia, C.-H., Chau, W., Zhang, Y., & Kwok, S. 2014, *Astrophys. J.*, 787, 25
- Hsia, C.-H., Sadjadi, S., Zhang, Y., & Kwok, S. 2016, *Astrophys. J.*, 832, 213
- Ishihara, D., et al. 2010, *Astron. Astrophys.*, 514, A1
- Ivezic, Z., Nenkova, M., & Elitzur M. 1999, DUSTY user manual, University of Kentucky internal report
- Jourdain de Muizon, M., Geballe, T. R., D'Hendecourt, L. B., et al. 1986, *Astrophys. J. Lett.*, 306, 105
- Jourdain de Muizon, M., D'Hendecourt, L. B., & Gabelle, T. R. 1990, *Astron. Astrophys.*, 227, 526
- Kimeswenger, S., & Barria, D. 2018, *Astron. Astrophys.*, 616, L2
- Knapp, G. R., Bowers, P. F., Young, K., & Phillips, T. G. 1995, *Astrophys. J.*, 455, 293
- Kwok, S., Hrivnak, B. J., & Langill, P. P. 1993, *Astrophys. J.*, 408, 586
- Kwok, S., Volk, K., & Hrivnak, B. J. 1999, *Astron. Astrophys.*, 350, 35
- Kwok, S., & Su, K. Y. L. 2005, *Astrophys. J. Lett.*, 635, 52
- Kwok, S. 2007, *Physics and Chemistry of the Interstellar Medium* (Sausalito, CA:Univ. Science Books)
- Kwok, S. 2010, *Proc. Astron. Soc. Aust.*, 27, 174
- Kwok, S., Chong, S.-N., Hsia, C.-H., et al. 2010, *Astrophys. J.*, 708, 93
- Lawlor, T. M., & MacDonald, J. 2002, in *Exotic Stars as Challenges to Evolution*, ed. C. A. Tout, & W. Van Hamme, ASP Conf. Ser., 279, 193
- Le Bertre, T., & Lequeux, J. 1992, *Astron. Astrophys.*, 255, 288
- Leuenhagen, U., & Hamann, W.-R. 1998, *Astron. Astrophys.*, 330, 265
- Likkel, L., Forveille, T., Omont, A., & Morris, M. 1988, *Astron. Astrophys.*, 198, L1
- Likkel, L., Morris, M., Kastner, J. H., et al. 1994, *Astron. Astrophys.*, 282, 190
- López, J. A., Meaburn, J., Bryce, M., & Holloway, A. J. 1998, *Astrophys. J.*, 493, 803
- López, J. A., García-Díaz, M. T., Steffen, W., Riesgo, H. & Richer, M. G. 2012, *Astrophys. J.*, 750, L131
- Lutz, J., Fraser, O., McKeever, J., & Tugaga, D. 2010, *Publ. Astron. Soc. Pac.*, 122, 524
- Manchado, A., Stanghellini, L., & Guerrero, M. A. 1996, *Astrophys. J.*, 466, L95
- Manchado, A., García-Hernández, D. A., Villaver, E., et al. 2011, in ASP Conf. Ser. 445, *Why Galaxies Care About AGB Stars II*, ed. F. Kerschbaum, T. Lebzelter, & B. Wing (San Francisco, CA:ASP). 161
- Manick, R., Miszalski, B., & McBride, V. 2015, *Mon. Not. R. Astron. Soc.*, 448, 1789
- Mastrodemos, N., & Morris, M. 1998, *Astrophys. J.*, 497, 303
- Meixner, M., Skinner, C. J., Temi, P., et al. 1993, *Astrophys. J.*, 411, 266
- Moshir, M., Kopman, G., & Conrow, T. A. O. (ed.) 1992, *IRAS Faint Source Survey, Explanatory Supplement Version 2*
- Nagata, T., Tokunaga, A. T., & Sellgren, K., 1988, *Astrophys. J.*, 326, 157
- Rubio, G., Vázquez, R., Ramos-Larios, G., et al. 2015, *Mon. Not. R. Astron. Soc.*, 446, 1931
- Sabin, L., Vázquez, R., López, J. A., et al. 2012, *RMxAA*, 48, 165

-
- Sahai, R. 2000, *Astrophys. J. Lett.*, 537, 43
- Sahai, R., Morris, M. R., & Villar, G. G. 2011, *Astron. J.*, 141, 134
- Santander-García, M., Rodríguez-Gil, P., Hernandez, O., et al. 2010, *Astron. Astrophys.*, 519, A54
- Shibata, K. M., Tamura, S., Deguchi, S., et al. 1989, *Astrophys. J. Lett.*, 345, L55
- Stanghellini, L., Bucciarelli, B., Lattanzi, M. G., & Morbidelli, R. 2017, *New Astron.*, 57, 6
- Steffen, W., Koning, N., Wenger, S., Morisset, C., & Magnor, M. 2011, *IEEE Trans. Vis. Comput. Graphics*, 17, 454
- Steffen, W., Koning, N., Esquivel, A., et al. 2013, *Mon. Not. R. Astron. Soc.*, 436, 470
- Su, K. Y. L., Kelly, D. M., Latter, W. B., et al. 2004, *Astrophys. J. Suppl. Ser.*, 154, 302
- van der Hucht, K. A., Conti, P. S., Lundstrom, I., et al. 1981, *Space Sci. Rev.*, 28, 227
- Vázquez, R., Miranda, L. F., Olguín, L., et al. 2008, *Astron. Astrophys.*, 481, 107
- Velázquez, P. F., Raga, A. C., Riera, A., et al. 2012, *Mon. Not. R. Astron. Soc.*, 419, 3529
- Wright, E. L., Eisenhardt, P. R. M., Mainzer, A. K., et al. 2010, *Astron. J.*, 140, 1868
- Weidmann, W. A., & Gamen, R. 2011, *Astron. Astrophys.*, 526, A6
- Zhang, C. Y., & Kwok, S. 1991, *Astron. Astrophys.*, 250, 179